



Schweizerischer Erdbebendienst
Service Sismologique Suisse
Servizio Sismico Svizzero
Swiss Seismological Service

ETH zürich

SITE CHARACTERIZATION REPORT

SFEL: Paul Scherrer Institut (AG), SwissFEL

Paolo Bergamo, Manuel Hobiger, Clotaire Michel, Donat Fäh



Last modification: 09.12.2016

Schweizerischer Erdbebendienst (SED)
Service Sismologique Suisse
Servizio Sismologico Svizzero
Servizi da Terratrembels Svizzer

ETH Zurich
Sonnegstrasse 5
8092 Zuerich
Schweiz
paolo.bergamo@sed.ethz.ch

Contents

	Section	Page
	Summary	3
1.	Introduction	4
2.	Geological setting	4
3.	Active seismic measurements	5
3.1	Equipment	6
3.2	Geometry of the acquisition arrays	7
3.3	Acquisition	8
3.4	Processing	9
3.4.1	<i>Pre-processing</i>	9
3.4.2	<i>P-wave refraction processing</i>	11
3.4.3	<i>MASW processing</i>	13
3.4.4	<i>WaveDec Active</i>	16
3.5	P-wave refraction interpretation	19
4.	Passive seismic measurements	20
5.	Rayleigh Wave Data Inversion	20
5.1	Misfit function	21
5.2	Parameterization of the model space	21
5.3	Inversion results	22
6.	Interpretation of the velocity profiles	23
6.1	Velocity profiles	23
6.2	Quarter-wavelength representation	25
6.3	SH transfer function	26
7.	Conclusions	27

Summary

The new SSMNet station SFEL has been installed (21.06.2016) in proximity to the new X-ray free-electron laser SwissFEL on the area of the Paul Scherrer Institut in the canton Aargau. Active seismic measurements, as well as a single-station noise recording survey, were performed to characterize the subsurface structure beneath the station. The main outcome is that the retrieved fundamental frequency is approximately 5.1 Hz, which is due to the impedance contrast between the gravelly alluvial terrace of the Aare (extending down to ~32 m depth), and the underlying, harder silt-sandstone layer. Further below (depths > 55 m), more compact rock layers are present, probably dolomitic marble and the upper portion of the Gipskeuper formation. The estimated V_{S30} value for the shallower subsurface is 551 m/s, which classifies the soil as class B.

1. Introduction.

In the framework of the second phase of the SSMNet (Swiss Strong Motion Network) renewal project, a new station, labelled as SFEL, was installed on 21.06.2016 in vicinity of the new X-ray free-electron laser SwissFEL at the Paul Scherrer Institut. SFEL is located on the right bank of the Aare river, resting on a gravelly alluvial terrace. As the station is surrounded by an area of thick tree coverage and unsuitable for the deployment of large arrays for noise recording, active seismic surveys were carried out to ensure the seismic characterization of the site. A single-station H/V measurement was performed as well to determine the fundamental frequency of the site.

2. Geological setting

The site is located in the valley of the Aare, on the right bank, and approximately 250 m far from the river. According to the geological information from the Swiss Office of Topography (swisstopo, see Figure 1), SFEL is placed on top of the gravelly alluvial terrace of the Aare (Niederterrassenschotter), whose thickness is expected to range between 20 and 55 m. Below, sandstone, siltstone, and dolomitic marble layers belonging to the Keuper formation are expected.

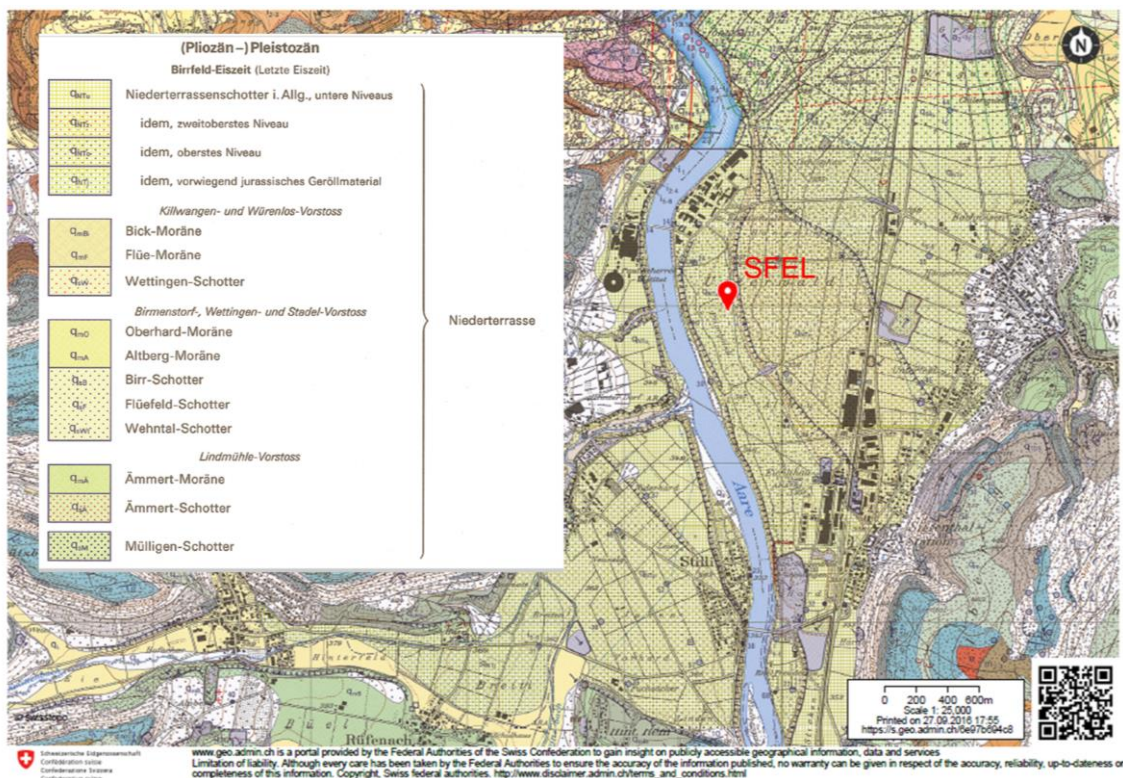


Figure 1 – Position of SFEL on the swisstopo Geological Atlas. For clarity of representation, we include only the portion of legend of interest for the area where SFEL is located (© 2016 Swisstopo, JD100042).

3. Active seismic measurements

The targeted station is located within the premises of the Paul Scherrer Institut. The facility occupies a linear strip of land within an area of dense, tall vegetation (Figure 2). This feature limits the applicability of passive seismic techniques (Michel et al., 2014), because of the difficulty in deploying a circular or circular-like array of sensors (with a diameter of tens of meters) in a forested area. Additionally, the trees may also negatively affect the GPS that ensures the synchronization and localization of the various sensors recordings. Consequently, the optimal choice appeared to be carrying out an active seismic survey with linear arrays deployed along the road running parallel to the accelerator. Two measurements were performed, on the same date (13/08/2016):

- i) The first measurement involved a receivers array 115 m long, the length being related to the aim of “reaching” the deep target of the bedrock depth (line 1 in Figure 1);
 - ii) The other seismic line is considerably shorter, 15 m long, placed in close proximity to SFEL. In this case, the aim was a detailed investigation of the shallower subsurface beneath SFEL.
- For the sake of a comprehensive subsurface characterization, for both seismic lines multichannel analysis of surface waves (MASW; Park et al., 1999) and P-wave refraction (Redpath, 1973) surveys were conducted.

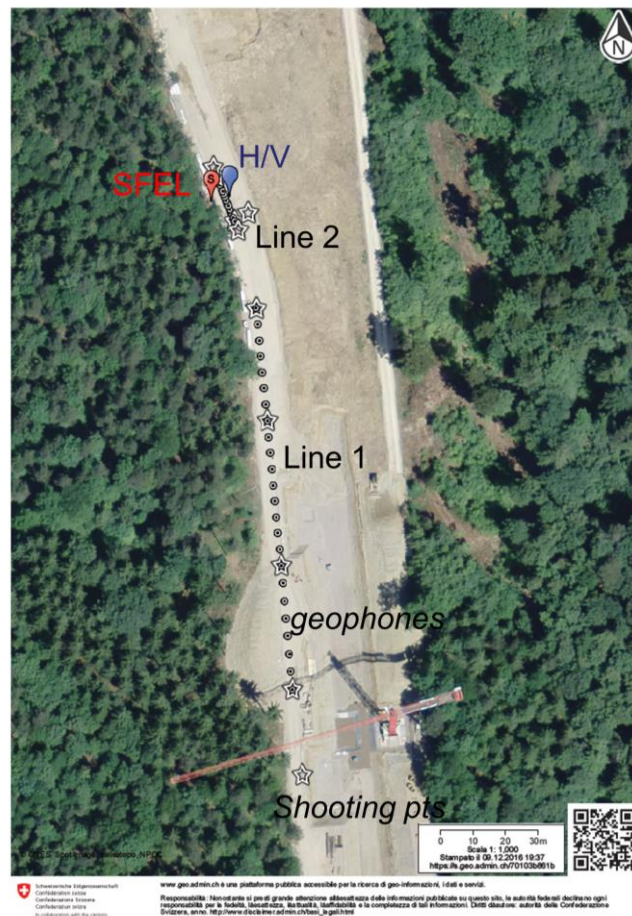


Figure 2 – Map representing the position of the targeted station (SFEL), of the two active seismic lines (line 1, line 2), and of the noise recording sensor (labelled H/V; © 2016 Swisstopo). The orthophoto available from Swisstopo was shot during the construction of the X-ray free-electron laser SwissFEL facility (completed at the time of execution of seismic measurements).

3.1 Equipment

As far as the first, longer seismic line is concerned (line 1 in Figure 2), we used three sets of eight three-component geophones (4.5 Hz corner frequency). Each geophone set was connected to a Geode datalogger; the three Geodes were coupled for time synchronization.

As for the seismic source, for the two off-end shots, considering the necessity to ensure signal coverage for a relatively long distance (maximum offset = 145 m), we used a weight drop device (Figure 3a), able to provide a greater energization when compared to the sledgehammer, which was used at the other shooting locations along the receivers spread (Figure 3c). The weight drop device is constituted by an outer frame and a hoist that allows lifting and suddenly releasing a mass made up of stacked metal bars. This mass drops freely and then hits a metal base placed on the ground. Considering previous experiences for the use of this equipment (e.g. Michel et al., 2013; Poggi et al., 2013), we used a dropping mass of 120 kg falling from an height of 1.3 m. Figures 3b and 3d compare the seismic traces (vertical component) obtained when using the weight drop or the 5-kg sledgehammer hitting a metal plate. The coherent seismic signal generated by the weight drop is indeed more energetic and clear, also at long offsets. As shown in Figure 3e, the energy of the seismic traces recorded using the weight drop is greater, by two orders of magnitudes, than using the sledgehammer. The drawback for the use of the weight drop equipment is that its assembling, de-assembling and redeploying are time-consuming and laborious.

As far as the shorter seismic line is concerned (line 2 in Figure 2), we used two sets of eight three-component geophones (4.5 Hz corner frequency). Here again, each geophone set was connected to a Geode datalogger; the two Geodes were coupled for time synchronization. The used seismic source was the 5-kg sledgehammer hitting a metal plate (Figure 3c).

For both seismic lines, the synchronization between the recorded traces and the seismic source was ensured by a trigger device fastened either to the hammer handle or to the outer frame of the weight drop.

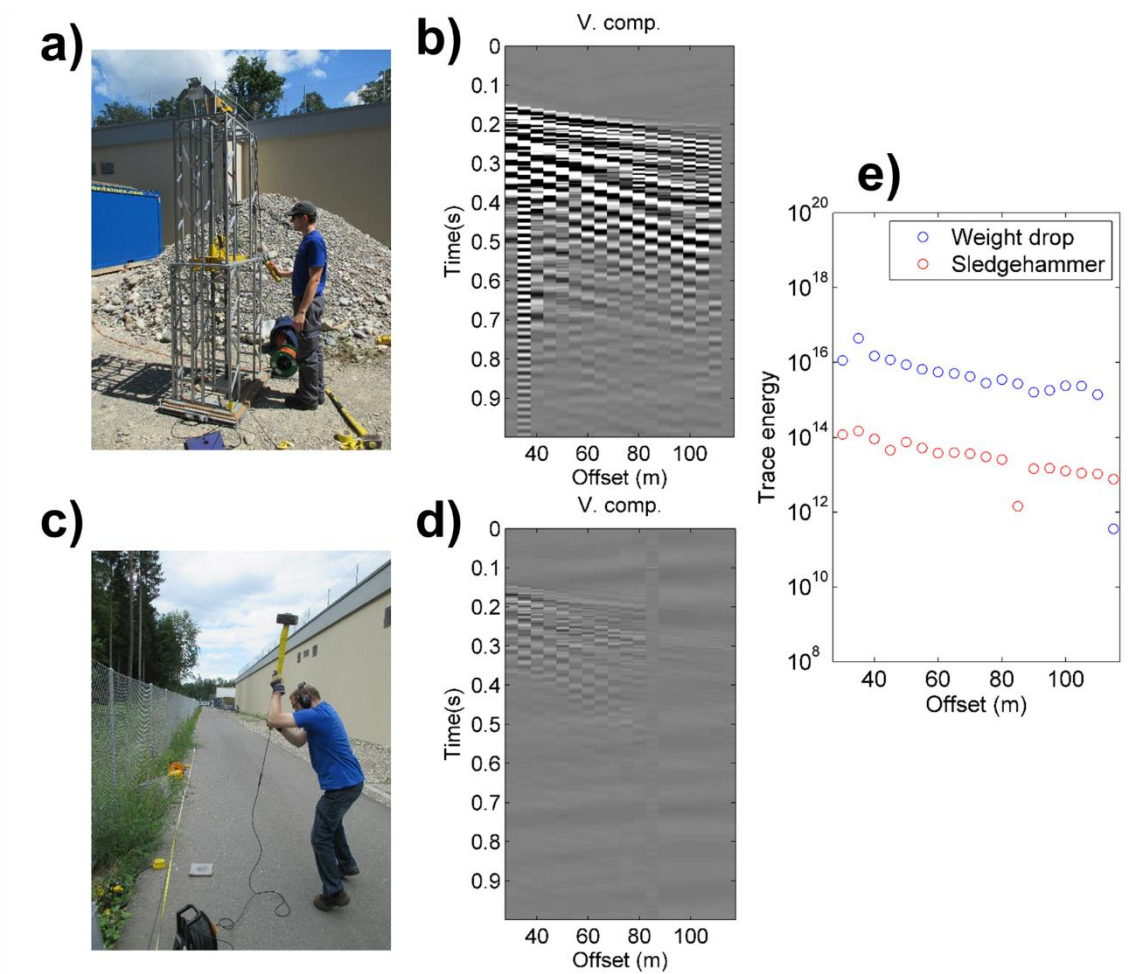


Figure 3 – Comparison of the employed seismic sources. a) weight drop device; b) sample seismic section (vertical component) obtained with the use of the weight drop equipment; c) sledgehammer; d) sample seismic section (vertical component) obtained with the use of the sledgehammer as seismic source. Note that the color scale for the amplitudes is the same of (b). e) energy of seismic traces shown in (b) and (d).

3.2 Geometry of the acquisition arrays

Line 1, whose receiver spread extends for 115 m, could not be deployed close to SFEL station, as a linear stretch of free space of adequate length was available only slightly south of the station itself (the distance between SFEL and the centre of the line 1 is about 95 m). As anticipated in 3.1, the receivers array was constituted by 24 3-component geophones, aligned at regular intervals of 5 m. The geophones were placed on the tarmac surface of the road (see Figure 3c). The length of the array was determined by the need to acquire surface wave wavelengths whose propagation is significantly affected by the presence of the bedrock (Socco and Strobbia, 2004), known from available geological information to be at a depth of about 45 m (Klinge, 2012). On the other hand, the relatively long inter-geophone distance ($\Delta x = 5$ m) limits the possibility to investigate the very shallow subsurface (the minimum recordable wavelength being Δx , Socco and Strobbia 2004). Consequently, a second line (line 2), shorter but with a smaller inter-receiver distance ($\Delta x = 1$ m), was deployed in close

proximity to SFEL station. Here again, the geophones were placed on the tarmac surface of the road. Line 2 was 15 m long (being constituted of 16 geophones): this allowed an adequate overlapping interval between the minimum wavelengths detected by line 1 and the maximum wavelengths from line 2.

At both lines, MASW and P-wave refraction measurements were performed. As for MASW surveys, the source was placed externally to the receiver spread, and at both ends (symmetrical off-end shooting configurations). For line 1, the minimum source-to-receiver offset was 30 m; 3 m in case of line 2. On the other hand, for P-wave refraction acquisitions, the source was deployed along the geophone line,

- at both ends of the receiver spread, for both line 1 and 2, and
- at two additional locations, at approximately one and two thirds of the array, for line 1 only (Figure 2).

In one case only (MASW acquisition on line 1, the source being located north of the array), the seismic source (sledgehammer or weight drop) was placed in contact with the soil surface (Figure 3a); in all other cases, the source was deployed on the tarmac surface of the road (Figure 3c).

3.3 Acquisition

Table 1 reports the parameters of time sampling adopted for MASW and P-wave refraction surveys. At each source point, 10 hammer/weight-drop blows were successively shot; at each shot, the recordings from all geophones were saved in a separate .sg2 file. In Figure 4, sample seismic sections representing the vertical component of recordings from MASW or refraction acquisitions are displayed. Seismic signals of interest (surface wave train, labelled “SW”, and P-wave first break arrivals, labelled “P”) are clearly recognizable. However, in the seismogram for P-wave refraction (Figure 4b), first break arrivals tend to “fade” at an offset of about 70 m, as the used sledgehammer source doesn’t seem to be able to ensure an adequate S/N ratio at large offset.

Table 1 – time sampling parameters

Line	Survey type	Sampling interval	Recording length	Pre-trigger delay
Line 1	MASW	125 μ s	1.75 s	-0.1 s
	Refraction	62.5 μ s	1 s	-0.1 s
Line 2	MASW	62.5 μ s	0.45 s	-0.1 s
	Refraction	62.5 μ s	0.45 s	-0.1 s

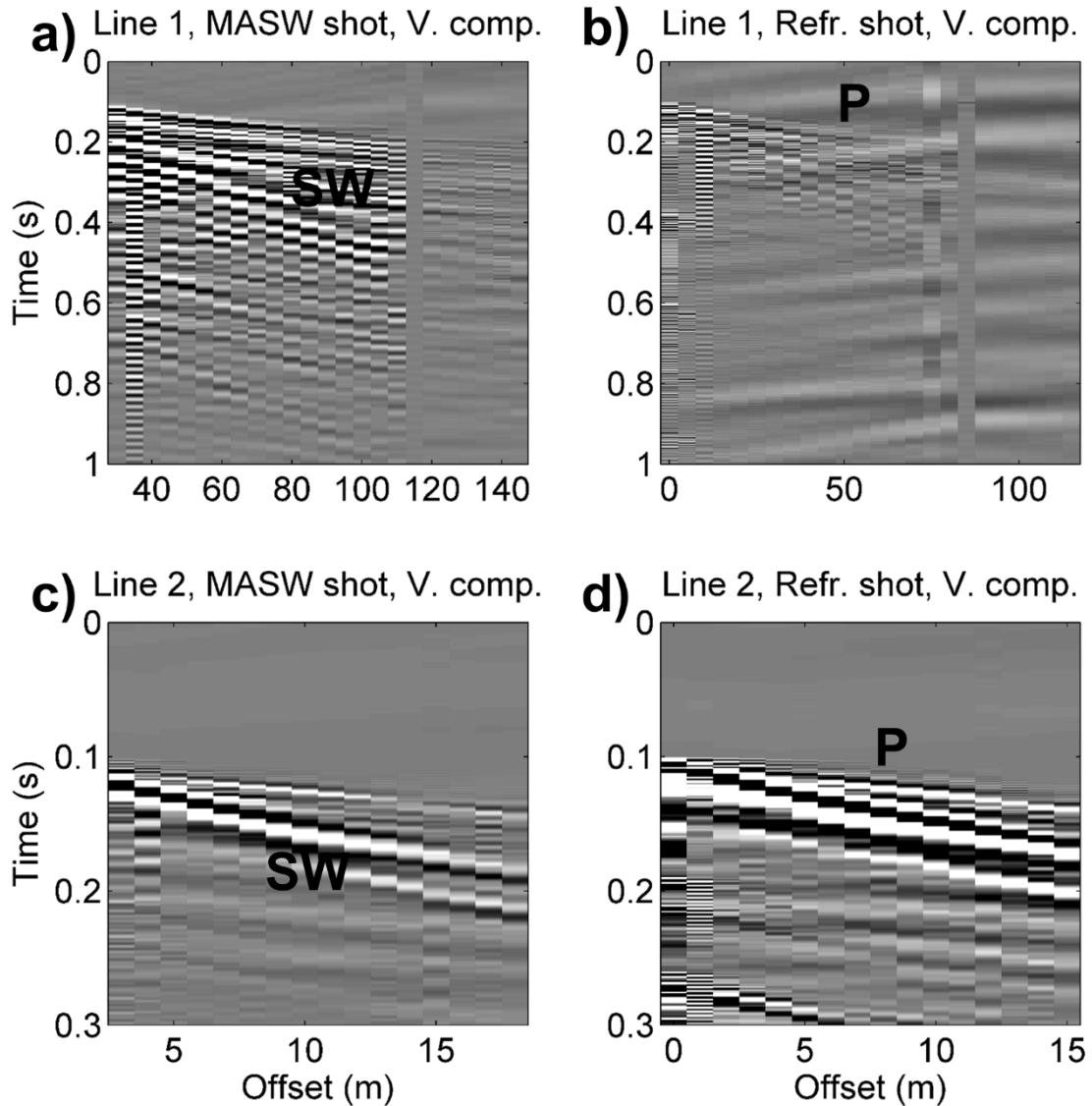


Figure 4 – Sample seismic sections (vertical component) acquired by line 1 (4a, 4b) and line 2 (4c, 4d), for the purpose of surface wave data analysis (4a, 4c) and P-wave refraction interpretation (4b, 4d).

3.4 Processing

3.4.1 Pre-processing

Seismic traces generated by different shots, where seismic source was positioned at the same location, were summed - or stacked - in time domain. This is done to enhance the coherent seismic events generated by the controlled seismic source, and at the same time to minimize the uncoherent noise anyhow present in the recordings (Foti et al., 2015). “Stacked” seismic sections, with greater signal-to-noise ratio, were hence obtained (Figure 5). To preserve the effectiveness of the stacking operation, the vertical components of the seismic traces at short offsets were cross-correlated to ensure an adequate synchronization among the seismograms to be later superimposed (Figure 6). The small

shifts among raw traces that are evident in Figure 6a can be ascribed to a non-ideal behavior of the trigger device.

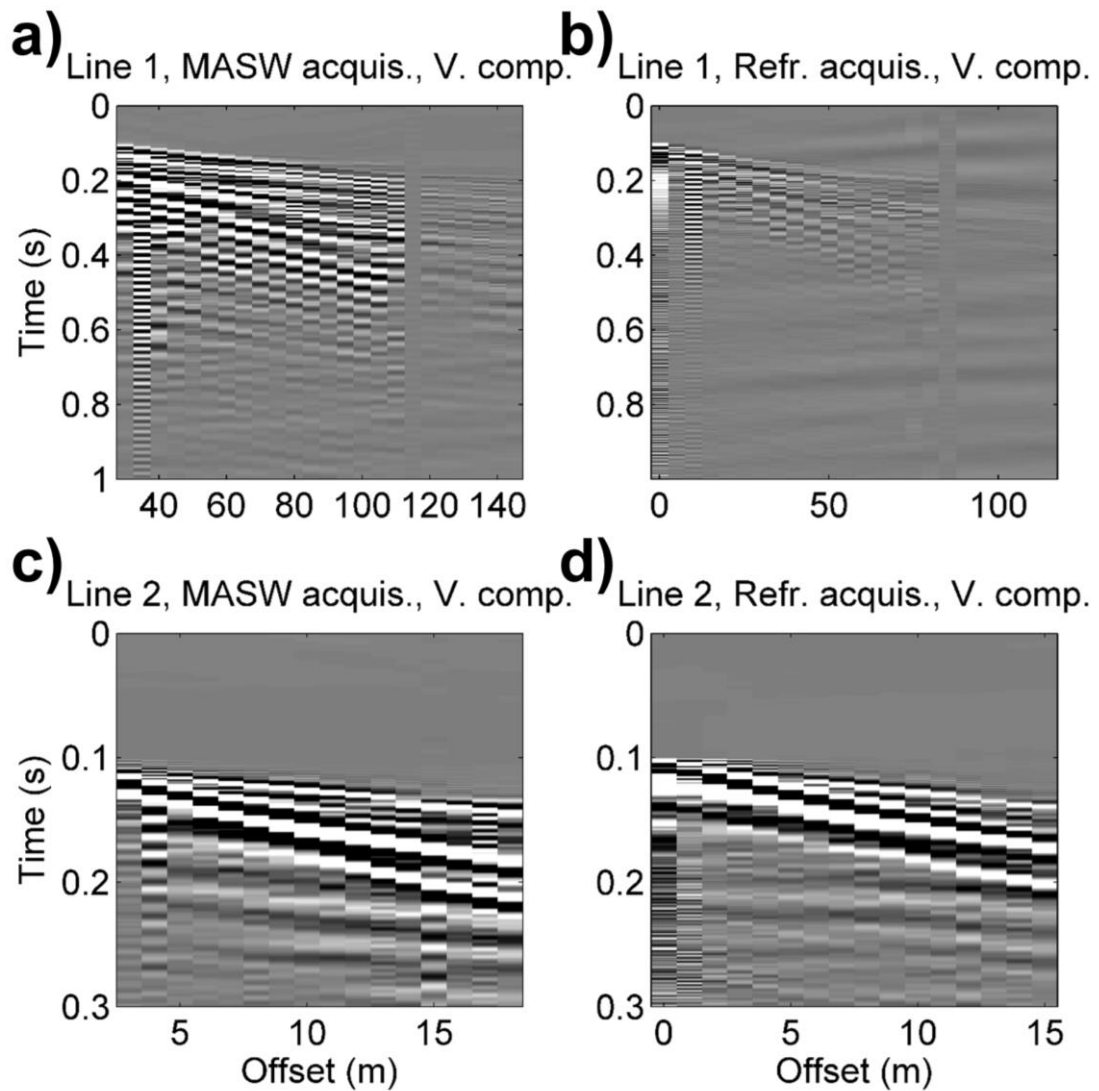


Figure 5 – “Stacked” seismic sections obtained by summing the (10) seismograms acquired with the same source-receiver configuration. Note that 5a-d correspond to 4a-d, but the latter represent single-shot sections.

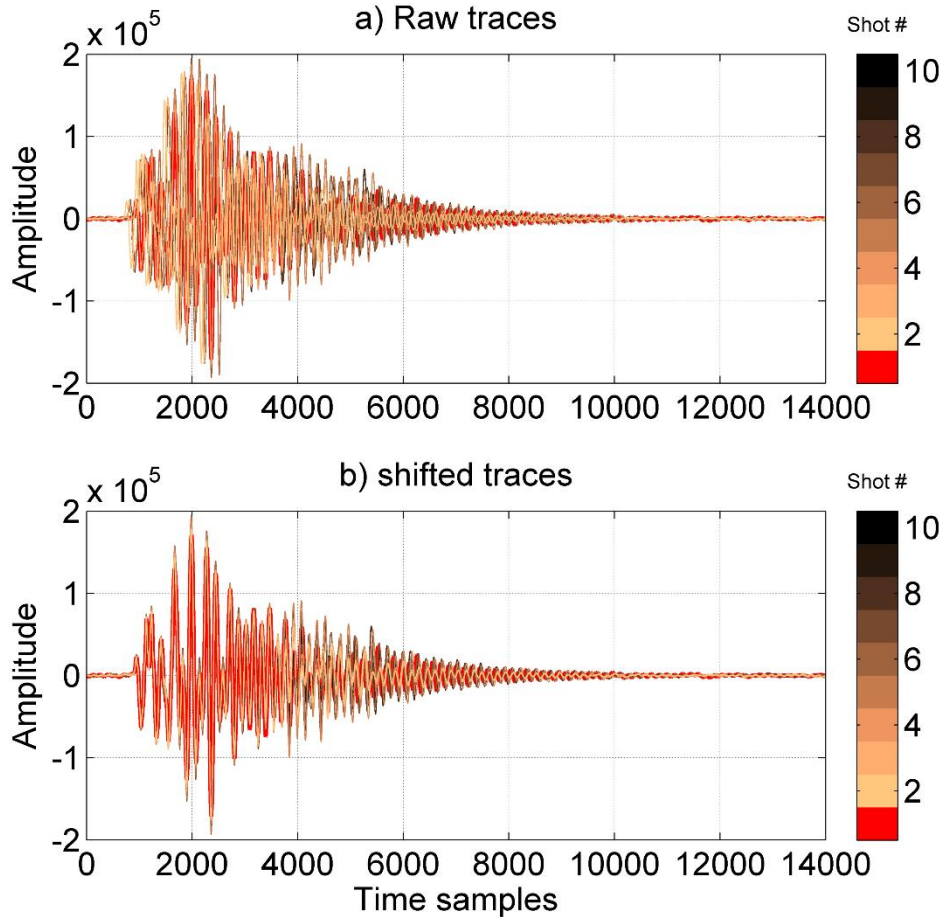


Figure 6 – Retrieving the optimal synchronization among seismic traces before stacking. a) raw seismic traces (vertical component) recorded at offset = 30 m at the 10 different shots carried out by positioning the source at the MASW shot point north of line 1; b) synchronized traces after the shifts for an optimal synchronization were retrieved via cross-correlation.

3.4.2 P-wave refraction processing

P-wave first-break arrival times were manually picked on the stacked seismograms representing the vertical component of soil surface vibration. Figure 7 represents the seismic sections on which the picking operation was carried out, as well as the picked travel time curves, or hodocrones (blue circles). Particularly in the case of the recordings from line 1, P-wave first break arrivals are hidden by a coherent seismic event with a velocity of approx. 1250 m/s (green crosses in the top left panel), which can be ascribed to the propagation of a guided wave through the thin tarmac layer. Hence, the picking had to be performed with great care.

As shown in Figure 8, the hodocrones appear to be approximately symmetrical, i.e. the P-wave travel time depends only on the source-to-receiver distance and not on the position of the shot point. This suggests a 1D geometry (no lateral variations) for the subsurface below the active seismic arrays.

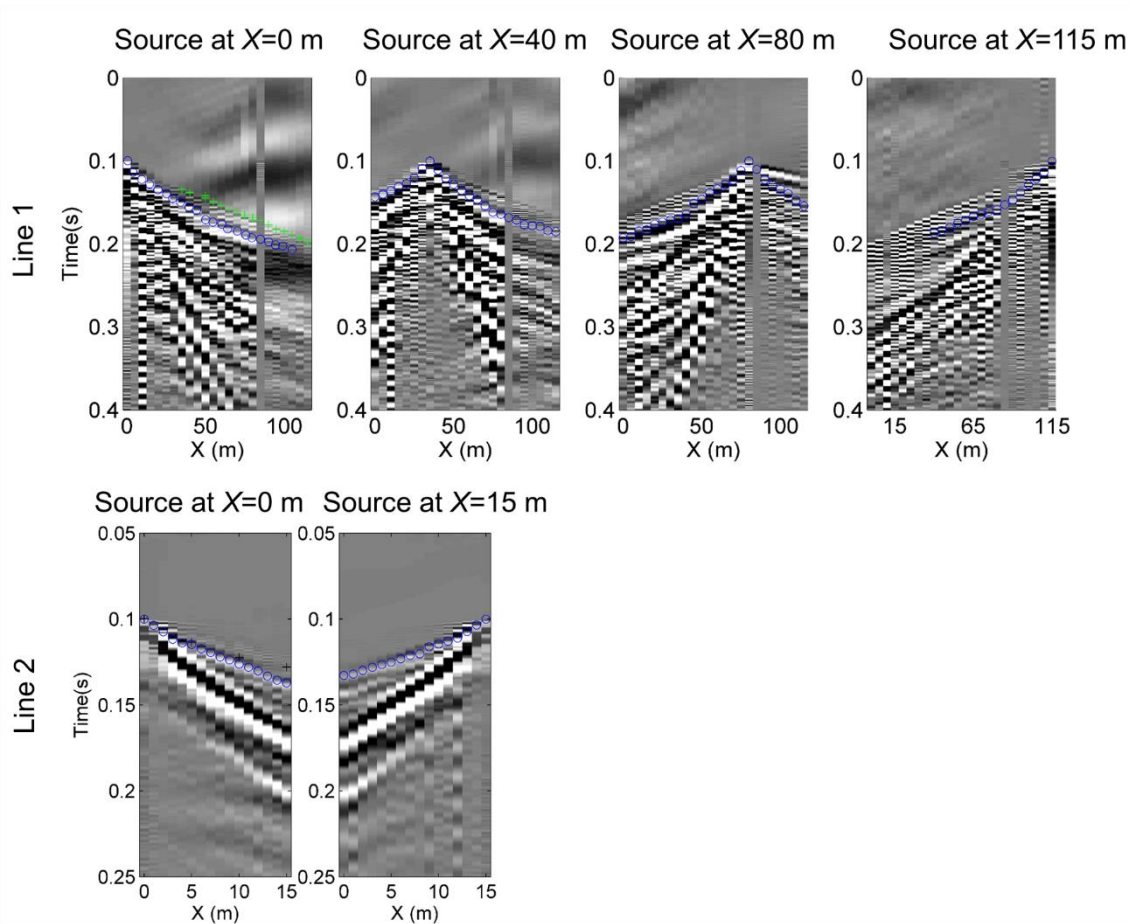


Figure 7 – Picking of P-wave first break arrival times (blue circles) on vertical component seismograms obtained after the stacking of raw traces. The X coordinate reference system is relative to each seismic line, and it progresses from north (first geophone, $X = 0$) to south.

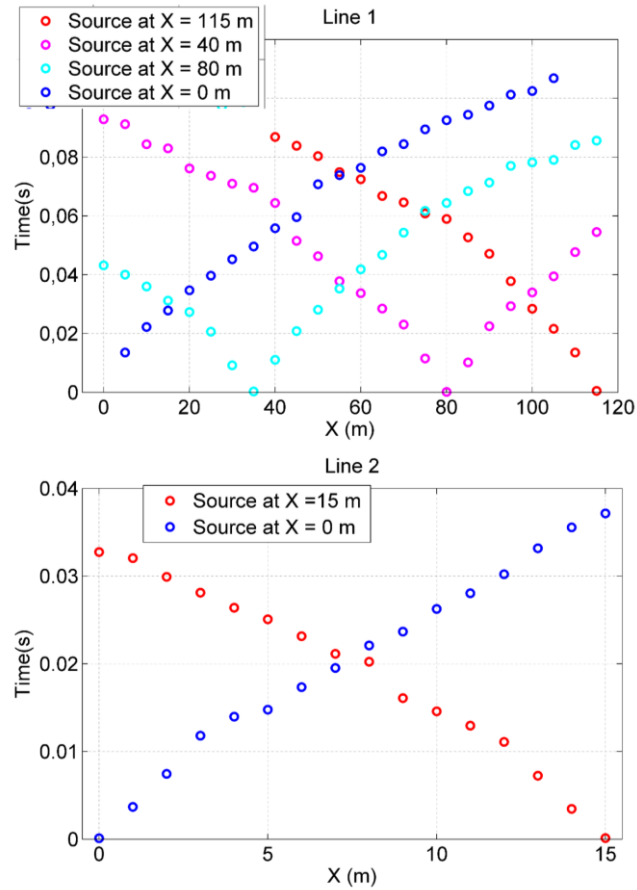


Figure 8 – Obtained P-wave travel-time curves. The reference system is the same as Figure 7.

3.4.3 MASW Processing

Vertical and longitudinal component seismograms from MASW acquisitions, considering both single shot and stacked seismic sections, were processed by means of a 2D $f-k$ (frequency – wavenumber) transform (Socco and Strobba, 2004), in order to obtain a conversion of the recorded sets of traces from time–offset to frequency–wavenumber domain. The energy maxima in the retrieved $f-k$ panels correspond to the propagation of Rayleigh waves and they depict the Rayleigh waves dispersive behavior (Socco and Strobba 2004, Foti et al., 2015). The maxima in the $f-k$ panels from stacked seismic sections were picked by manually defining regions of interest in the $f-k$ domain and then automatically identifying the peaks, frequency by frequency, within the selected areas (Figure 9). The defined regions of interest were also automatically applied to the $f-k$ spectra from single shot seismograms. Hence, for each shooting configuration and for each considered component (vertical or longitudinal) we obtained:

- i) one set of $f-k$ maxima, retrieved from the stacked seismic section, that defines the corresponding dispersion curve (circles in Figure 10a,b);
- ii) ten sets of $f-k$ maxima, each of them derived from a single shot seismogram, that define the experimental uncertainty for the dispersion curve introduced in i (dots in Figure 10a,b).

This processing procedure follows the scheme described by Socco et al. (2009) and Boiero and Socco (2010).

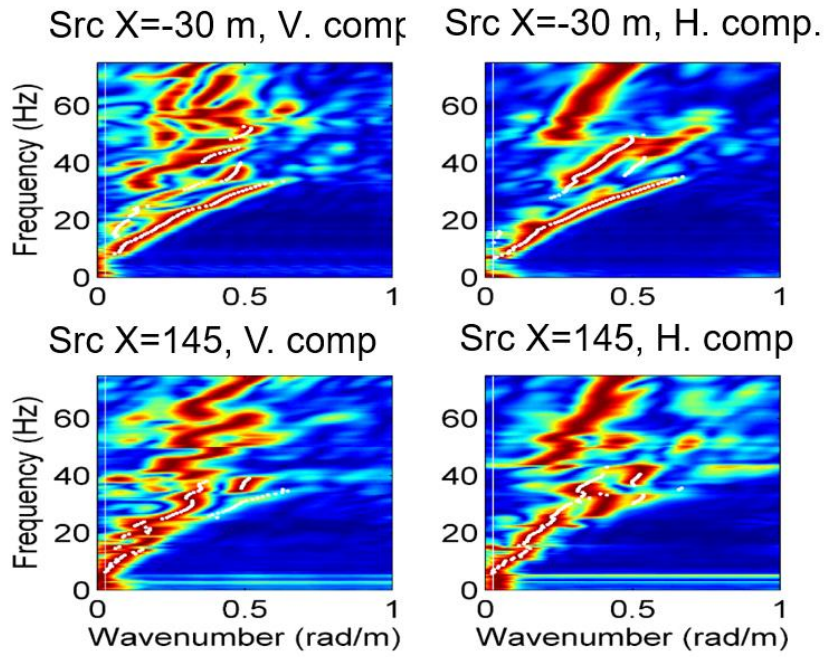
The dispersion curves from the four considered datasets (vertical and longitudinal components of the two off-end shootings) show good reciprocal consistency, aligning along coherent modal branches, for both lines 1 and 2 (Figure 10a, b). This similarity, particularly among curves from opposite shooting configurations, supports the hypothesis, inferred from the observation of P-wave travel times (3.4.2), of a substantially 1D geometry for the subsurface beneath the active seismic arrays.

Besides, when combined together (Figure 10c), the dispersion curves from line 1 and line 2 show a good reciprocal agreement, having similar phase velocities in the overlapping frequency band 30-50 Hz, for all the identified modal branches. This feature further confirms the lack of substantial lateral variations in the surveyed subsoil.

The agreement among the eight dispersion curves from stacked seismic sections (circles and triangles in Figure 10c) allows combining them, via averaging, into a single dispersion curve, representative of Rayleigh wave propagation in the subsoil below the active seismic arrays over a wide frequency range (6 - 110 Hz, Figure 10d). As earlier anticipated, the phase velocity data from single shot dispersion curves (dots in Figure 10a,b) were exploited to define the experimental uncertainties (error bars in Figure 10d, computed as the standard deviation of the relevant population of phase velocity data points).

The attribution of the dispersion curve branches to the fundamental, first and second higher modes (Figure 10d) was based on a simplified seismic model derived from the P-wave refraction interpretation (3.5).

Line 1



Line 2

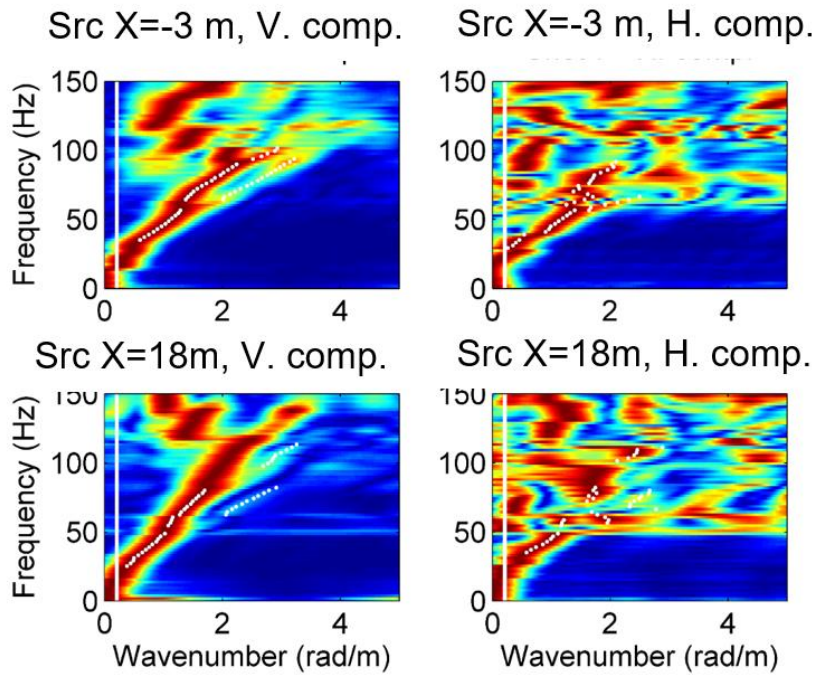


Figure 9 – Normalized f - k spectra obtained from vertical and longitudinal components of stacked seismic sections of MASW recording configurations.

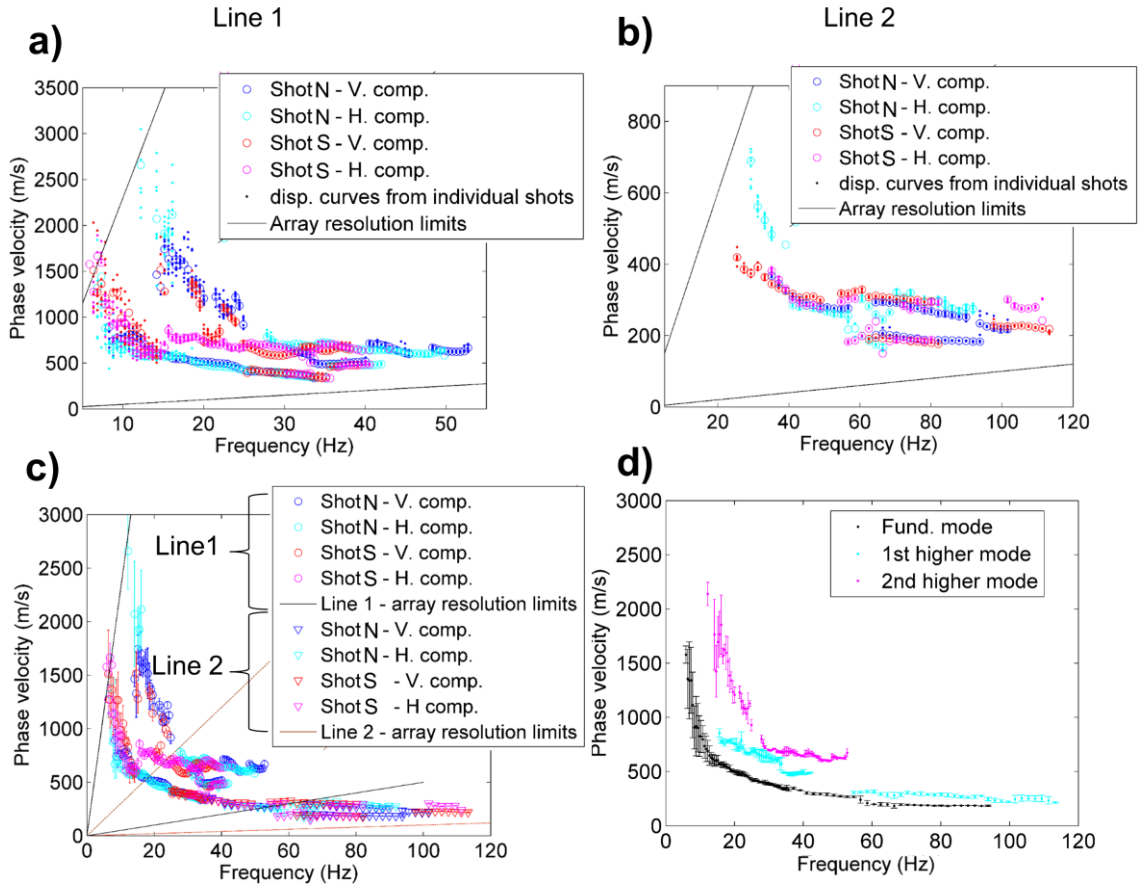


Figure 10 – Obtained dispersion curves. a) dispersion curves derived from stacked seismic sections (circles) and single shot seismograms (dots), line 1; “shot N” and “shot S” label the different recording configuration, the source being placed north or south of the receivers spread. b) same as (a) for line 2. c) dispersion curves derived from stacked seismic sections from both line 1 and 2; d) average global dispersion curve with uncertainties.

3.4.4 WaveDec active

Active recordings acquired by line 1, with the source being positioned at the two MASW shot points north and south of the array, were also processed with the WaveDec Active code (Maranò et al., 2016). WaveDec Active implements a maximum likelihood algorithm for the analysis of Rayleigh waves generated by a controlled source. Differently from the more conventional $f-k$ analysis approach (3.4.3), it is able to characterize the Rayleigh wave propagation both in terms of phase velocity and ellipticity angle. Key parameters required by WaveDec Active are the definition of the maximum number of Rayleigh waves that the code attempts to identify, and the value of parameter γ , which is able to modify the approach of the code towards wave identification from a Bayesian information criterion ($\gamma=1$) to a maximum likelihood approach ($\gamma=0$), or a compromise between the two ($0<\gamma<1$). Following the recommendations of the code’s author (Maranò 2016) and some preliminary attempts, the maximum number of waves was set to 3, and γ to 0.3, thus opting for an approach relatively close to a maximum likelihood solution. Seismic traces acquired by a geophone with a defective vertical component channel (at X = 80 m) were removed from the input data fed to the code, as the processing

output of WaveDec Active proved to be quite sensitive to the presence of imperfect traces. The obtained results are displayed in Figure 11, showing the estimated Rayleigh wave phase velocities (Figure 11a, c) and ellipticity angle (Figure 11b,d) for the considered shots.

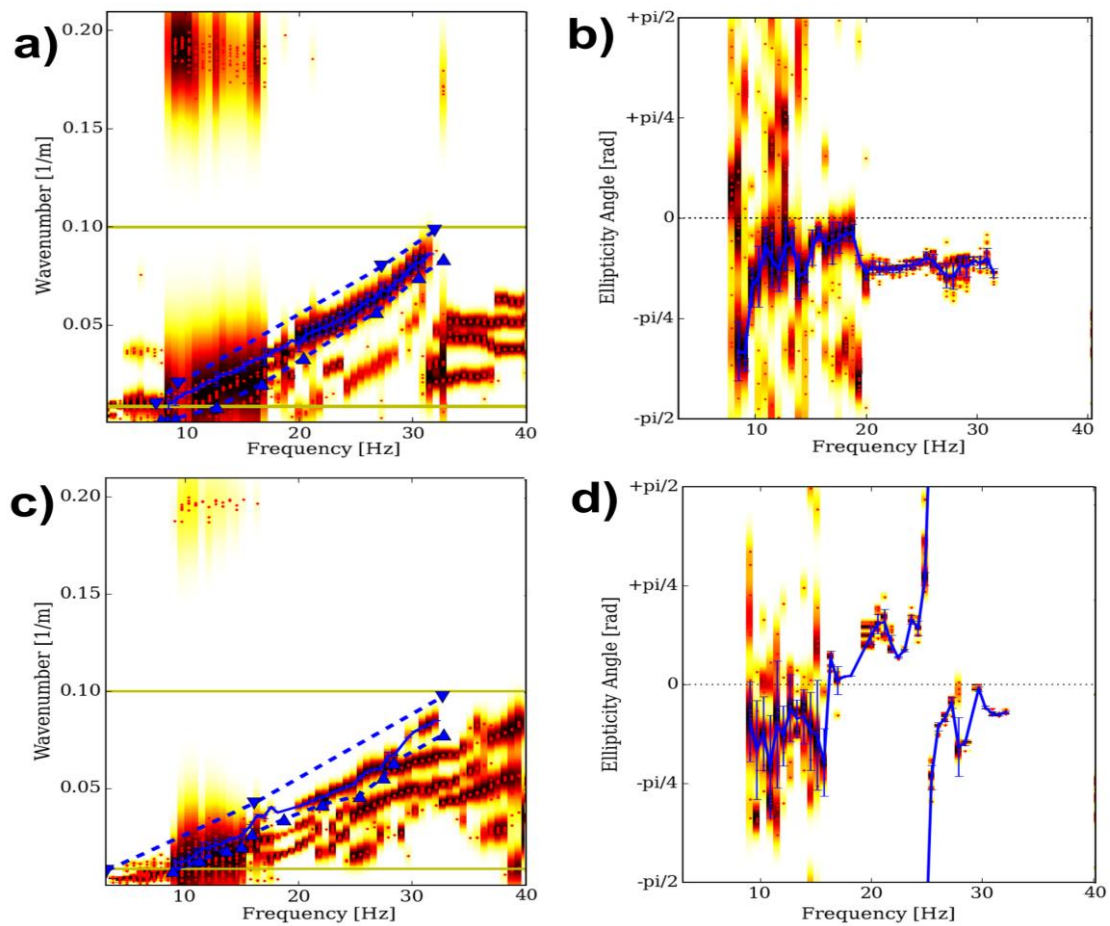


Figure 11 – WaveDec Active processing results. Estimated Rayleigh wave wavenumbers (a) and ellipticity angles (b) from the 3C seismic traces recorded by line 1, the source being located north of the array. Estimated wavenumber/ellipticity values are represented as red dots, whose density in the distribution across the velocity/frequency or ellipticity angle/frequency panel corresponds to the shaded colours. Golden lines define the array resolution limits as defined in WaveDec Active code. The continuous blue line indicates the median of the wavenumber values identified by the operator as fundamental mode (operator’s selection is represented by blue dashed lines). In (b), only the ellipticity values corresponding to the selection in the wavenumber-frequency domain (a) are represented. c,d) same as (a,b), but from the 3C seismic traces recorded by line 1, the source being located south of the array.

In both panels 11a and 11c the Rayleigh wave fundamental mode was easily recognizable, in the frequency band 8-35 Hz. The fundamental mode was then selected, using the WaveDec Active picking tool (dashed blue lines in Figures 11a, 11c). As displayed in Figure 12c, phase velocity values obtained from WaveDec Active and from the f-k analysis (3.4.3) are consistent. Vice versa, the corresponding ellipticity values are significantly lower (Figure 12b) than those estimated from passive noise recordings (section 4), witnessing an apparent marked prevalence of the vertical over the horizontal component of Rayleigh waves. This feature could be ascribed to the non-optimal ground-receiver coupling of the active lines; in fact, for logistical reason, geophones had to be placed

on the tarmac surface of the road close to SFEL station (Figures 3a, 3c), therefore lacking a firm anchoring to the subsoil (generally ensured by metal spikes penetrating the ground). For comparison, in Figure 13 we show the trace energy from the vertical and longitudinal components of active seismic arrays, from the considered SFEL survey and from another acquisition (SBIK SSMNet characterization survey, report in preparation), where the same geophones were coupled to the soil with spikes. In the left panel, the significantly greater distance between the energy for the vertical and longitudinal component traces suggests a non-ideal soil-receiver coupling. Hence, the obtained Rayleigh wave ellipticity curve cannot be considered reliable.

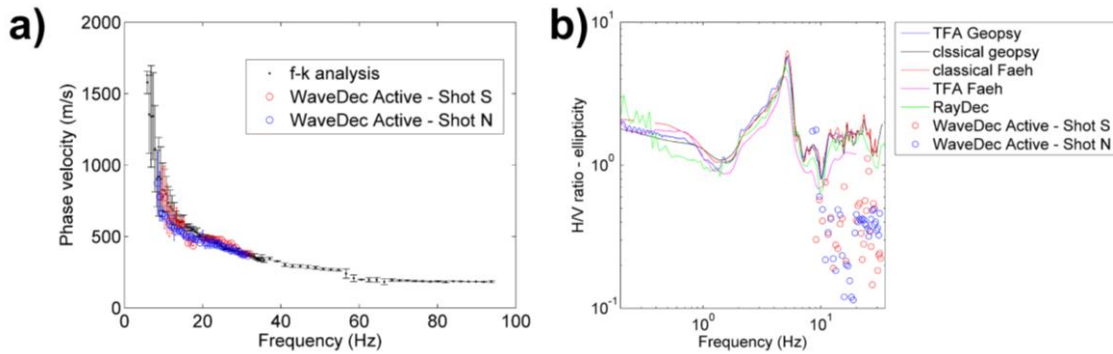


Figure 12 – Comparison of WaveDec Active results with other methods. c) comparison between the dispersion curve obtained from f - k processing (black dots) and the phase velocities estimated for the fundamental mode by WaveDec Active. d) comparison between the ellipticity curves obtained from passive data recordings (see section 4) and the estimated ellipticity values from WaveDec Active.

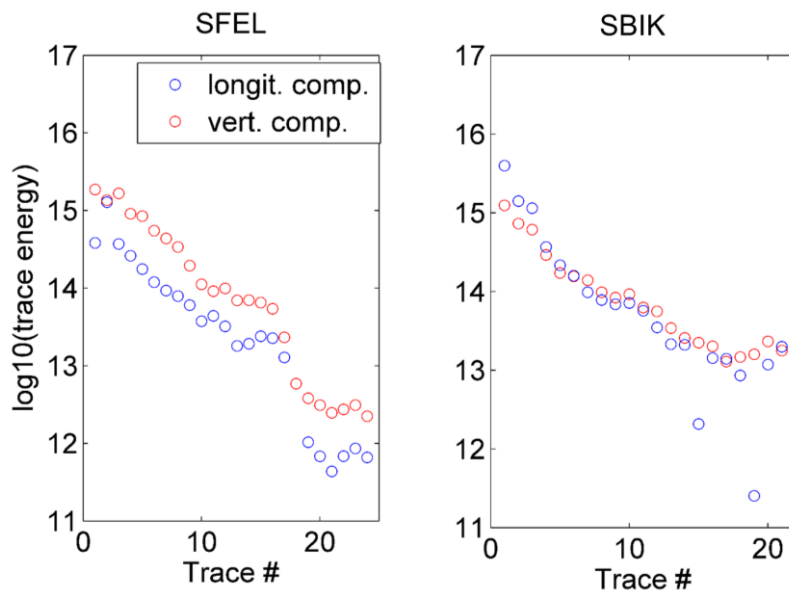


Figure 13 – Comparison between trace energy from the vertical and longitudinal components: left, from a sample seismic section for SFEL site, line 1; right, from an acquisition from another site (Biel Kongresshaus, SBIK) where the same geophones were firmly coupled to the ground with spikes. Note that in logarithmic scale the distance along the y -axis corresponds to the logarithm of the energy ratio between vertical and longitudinal component.

3.5 P-wave refraction interpretation.

P-wave refraction data (3.4.2) were interpreted with the method of intercept time analysis (Reynolds, 2011). Following the hypothesis of a 1D geometry for the shallow subsurface (3.4.2, 3.4.3), the hodocrones obtained from refraction processing were all collapsed in a single travel-time curve in time-offset domain (circles in Figure 14a). To ensure a longer offset coverage, and hence a larger investigation depth, travel times picked from the MASW seismic sections from line 1 were added as well. As for the intercept time interpretation, the identification of direct and refracted arrivals was based on the evaluation of the local slope of the travel time curve, obtained by shifting a 23 m wide moving window along the curve (Figure 14b). Hence the hodocrone was subdivided into five segments having different slopes (Figure 14a), corresponding to as many layers. The P-wave velocity model obtained thanks to the application of intercept time equations is shown in Figure 14c. The shallower subsurface appears to be composed by two layers, having $V_P = 255$ and 454 m/s and thicknesses of 0.3 and 1.8 m respectively. Below these surficial layers, P-wave velocity increases to 775 m/s until 14.1 m. Below this depth, V_P reaches 1480 m/s, probably indicating the presence of a saturated formation. The deepest layer to be identified has a V_P of 3400 m/s and its upper interface is at 35 m depth; this value coincides with the maximum investigation depth of the travel time analysis.

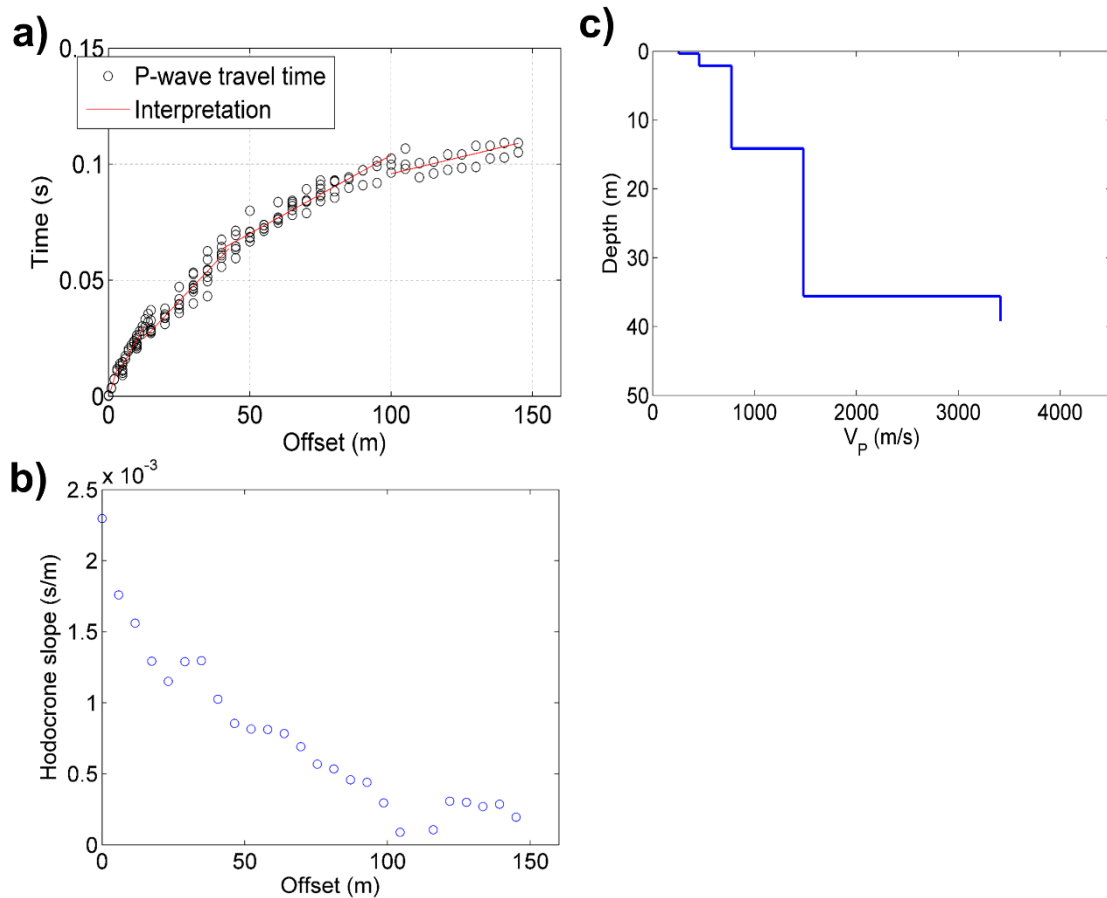


Figure 14 – P-wave travel time interpretation. a) travel time curves and piecewise linear fitting of the hodocrone segments. b) local slope of the travel time curve, evaluated with a moving window sliding along the offset axis. c) obtained P-wave velocity model.

4 Passive seismic measurements

Besides active seismic surveys, a single-station noise recording measurement was performed. A Lennartz 3C 5s seismometer, connected to a Quanterra Q330 datalogger, was deployed in close proximity to station SFEL (Figure 2). The sensor was placed on a metal tripod in a 10 cm deep hole, for a better coupling with the ground. The sampling frequency was 200 Hz, and the recording spanned an 8 hour time interval (in parallel to active surveys). The acquired traces were processed with the aim of

- estimating the H/V ratio of recorded noise, thus identifying the fundamental frequency of resonance of the site (Nakamura, 1989), thanks to the application of classical H/V methods (as implemented in Geopsy software, www.geopsy.org; classical H/V of Fäh et al., 2001).
- estimating the ellipticity of Rayleigh wave as a function of frequency, by resorting to refined algorithms (Raydec, Hobiger et al., 2009; time-frequency method, Poggi and Fäh, 2009; wavelet-based time-frequency method as implemented in Geopsy software). These methods aim at eliminating the contributions of other waves besides Rayleigh waves, to obtain a more reliable estimation of Rayleigh wave ellipticity when compared to the classical H/V technique.

The obtained results are shown in Figure 15. All applied techniques yield similar H/V or ellipticity curves, with a clear peak at 5 Hz, identifying the fundamental frequency of resonance of the site.

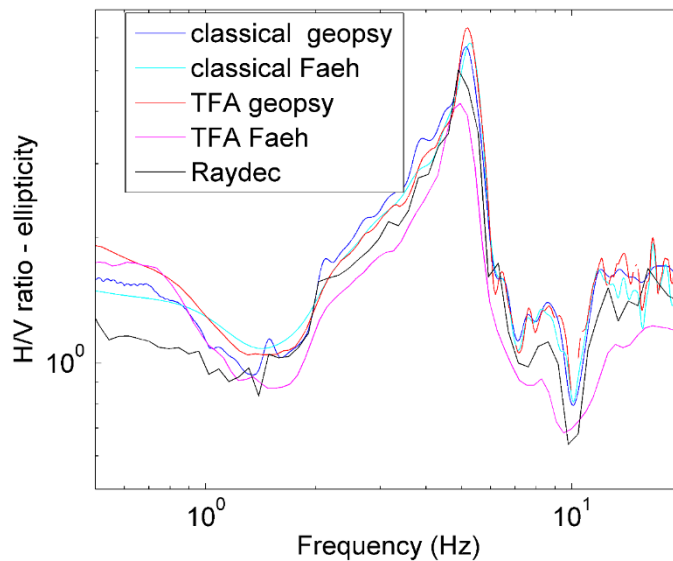


Figure 15 – H/V ratio and ellipticity curves obtained from the processing of noise recording data.

5 Rayleigh Wave Data Inversion

The retrieved phase velocity dispersion and ellipticity characteristics of Rayleigh waves (sections 3.4.3, 4) were inverted for a 1D profile of the seismic properties of the subsurface. The inversion was performed using the Dinver software of the Geopsy suite that implements an Improved Neighborhood Algorithm (Wathelet, 2008).

5.1 Misfit function

As anticipated, both the estimated Rayleigh wave dispersion and ellipticity curves were included in the inversion.

As for dispersion data, the dispersion curve obtained from the f - k analysis of active MASW measurements (3.4.3) was fed to the inversion software. Phase velocity uncertainties were taken into account. The dispersion curve is composed by three modal branches, identified as fundamental, first and second higher modes (Figure 10d). The fundamental mode spans without interruption a 6-95 Hz frequency band; higher modes extend across narrower intervals, yet they reach relatively low frequencies (16 Hz the first higher, 12 Hz, the second higher), thus potentially ensuring a high resolution estimate of the V_s profile in an extended depth range (Xia et al., 2003).

The ellipticity curve retrieved by applying the Raydec code on noise recordings (section 4) was used for the inversion. Ellipticity data were considered reliable within the 1-20 Hz frequency band; the lower limit was chosen considering that below such threshold the estimated ellipticity behavior differs significantly depending on the adopted algorithm. The ellipticity curve, comprehensive of standard deviations, was attributed to the fundamental mode of Rayleigh wave propagation, as within 1-20 Hz the fundamental mode appears to be dominant (see Figure 9, left panels). Data points in the 2-5.4 Hz and 7.5–10 Hz intervals were removed to allow for the presence of singularities (Hobiger et al., 2013). Comparison (not shown here) between inversions performed including or excluding this set of data points confirmed the goodness of this choice.

Both ellipticity and dispersion curves were resampled using 100 points between 0.5 and 135 Hz, on a logarithmic scale. The ellipticity information was given lower weight (0.1) when compared to the dispersion curve (1) in the contribution to the overall misfit value.

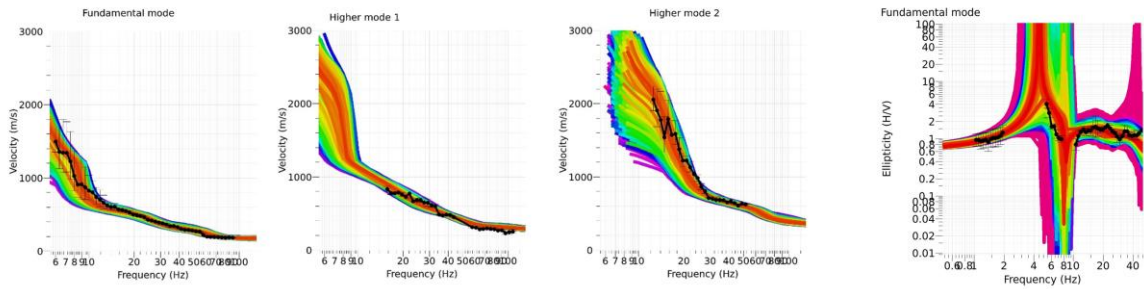
5.2 Parameterization of the model space

The parameterization of the shallower portion of the subsurface (until 35 m depth) was derived from the model retrieved from the interpretation of refraction data (see section 3.5). Interfaces depths and P-wave velocity values were left free to vary within constrained intervals centered on the obtained V_P profile. Preliminary inversion attempts showed the necessity to introduce an additional layer, between the 2 and 14 m depth interfaces of the V_P model from refraction, to adequately fit the dispersion curve points at high frequencies (> 30 Hz). As explained later in the text (section 6), this discrepancy can be attributed to the different sensitivity and depth coverage of the two techniques (surface wave method and refraction).

As for the deeper subsurface (from 35 m to the maximum investigation depth, approx. 90 m), this was alternatively modeled as a stack of two or three layers overlying a halfspace in two parallel inversion runs. In both cases wide velocity ranges but constrained thickness intervals were attributed to these deeper formations, as suggested in Burjanek et al. (2013a,b).

The Poisson's ratios were left free to vary within 0.2-0.4, with the exception of the intermediate layers (4th-5th layers), where the maximum limit was raised to 0.47 to allow for the presence of saturated layers (as suggested by the P-wave travel time analysis, section 3.5). Fixed density values increasing from 1600 (surficial layer) to 2500 kg/m³ (halfspace) were assigned.

8 layers, constr. thicknesses. Min. RMSE = 2.45



7 layers, constr. thicknesses. Min. RMSE = 2.42

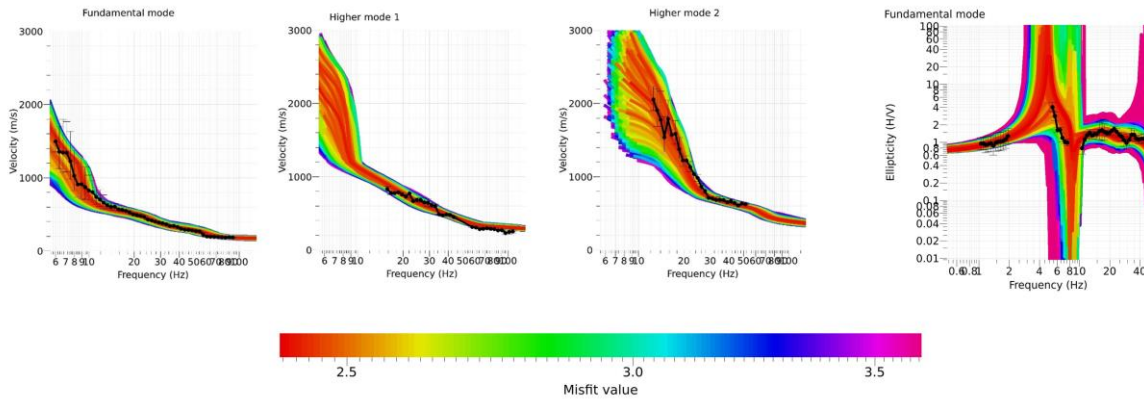


Figure 17– Inversion results. Comparison between experimental and synthetic curves for the profiles shown in Figure 16.

6 Interpretation of the velocity profiles

As anticipated in section 5.3, the parameterization involving 7 layers with constrained thicknesses was chosen as the most reliable representation of the subsurface structure. The best 15 performing profiles models (RMSE<2.5) are represented in Figure 18 and considered for the geological interpretation.

6.1 Velocity profiles

The shallowest layer (Figure 18) has a V_S of 183 m/s and a thickness of 1.2 m. Below, between 1.2 and 6 m depth, V_S increases to 380 m/s; at around 5.5 m S-wave velocity grows to 670 m/s, a value which is constant until a depth of 31-36 m. This interface marks a sharp change in the properties of the subsurface, as V_S and V_P increase from 670 to 1250-1650 and from 1600 to 2600-4000 m/s, respectively. This impedance contrast is responsible for the 5 Hz peak in the H/V and ellipticity curves (Figure 15). Below ~55 m depth, V_S reaches 1600-2600 m/s, and finally (depths>75 m) 2200-3000 m. It should be noted that the sensitivity towards the velocity of these two deepest formations is limited, so that at these depths the variability among feasible velocity values becomes significant. Among the 15 subsurface models shown in Figure 18, the lowest misfit configuration (thicker red line) was selected as final inversion result, and hence used for the analyses presented in the following

sections (6.2, 6.3). The V_{S30} for the chosen profile is 551 m/s, classifying the soil as type B according to Eurocode 8 (CEN, 2004) and SIA261 (SIA, 2014).

As for the geological interpretation of the retrieved seismic models, we refer to the stratigraphy identified by two borehole logs:

i) The first borehole was executed in 2012 for surveying purposes for the construction of the electron accelerator, at a location about 150 m south of the centre of line 1. The maximum depth is 40 m (Jäckli Geologie, 2012). Because of its proximity with performed measurements and station SFEL, this borehole is used as reference for the shallower portion of the seismic profiles. It is henceforth referred to as PSI borehole.

ii) The second borehole is part of the NAGRA borehole database. Reaching a depth of 1500 m, it was performed in 1985 in the municipality of Böttstein, 3.5 km north of station SFEL (NAGRA, 1985a,b). It is henceforth referred to as NAGRA borehole.

The shallowest layer (Figure 18; $V_S = 183$ m/s, thickness = 1.2 m) hence corresponds to the surficial soil cover. The layer below, between 1.2 and 5.5 m depth, is compatible in terms of seismic velocities and depth, when compared to PSI borehole, with the shallower part of the Niederterrassenschotter (gravelly alluvial terrace), which is the weathering formation for the investigated area, as reported by the Swiss Geological Atlas (Swisstopo, 2013), and by PSI and NAGRA boreholes. Following PSI borehole, this layer is constituted by light gravel mixed with sand and stones. It is worth remarking that for these shallow layers the V_P values determined by Rayleigh wave data inversion match the model retrieved with P-wave refraction. The deeper portion of the Niederterrassenschotter (depths between 6 and 31-36 m) is indicated to be to a more compacted sandy, silty gravel formation, according to PSI borehole; hence the V_S increase from 380 to 670 m/s reflects this greater level of compaction. It should be noted that in the depth range 6 – 14 m the V_P profiles from refraction interpretation and Rayleigh wave data inversion – otherwise reasonably similar – differ significantly, as the latter introduce an intermediate layer with P-wave velocity = 1150 m/s. This discrepancy can be probably ascribed to the fact that this additional layer does not produce a marked change in the P-wave travel time hodocrone slope, hence it was not identified in the refraction data interpretation. The dense wavelength coverage in this depth range by the multimodal Rayleigh wave dispersion curve, and the indication of PSI borehole, support anyway the existence of this intermediate layer. Proceeding downwards along the profiles, it is reasonable to assume that the portion of the Niederterrassenschotter at depths >12-14 m is water saturated, as retrieved V_P values increase towards ~1600 m/s, also in agreement with P-wave refraction results; this is also compatible with PSI borehole information (in August 2012, the water table was at 18 m depth). The layer underlying the gravelly alluvial terrace (depth 35 – 55 m) can be identified as the sandstone-siltstone formation with interleaved lenses of silt and clay from the NAGRA borehole. Further below, the two deepest layers (55 – 75 m depth and the halfspace) can be interpreted as dolomitic marble and the upper portion of the Gipskeuper formation, respectively, again according to the geological succession from NAGRA borehole.

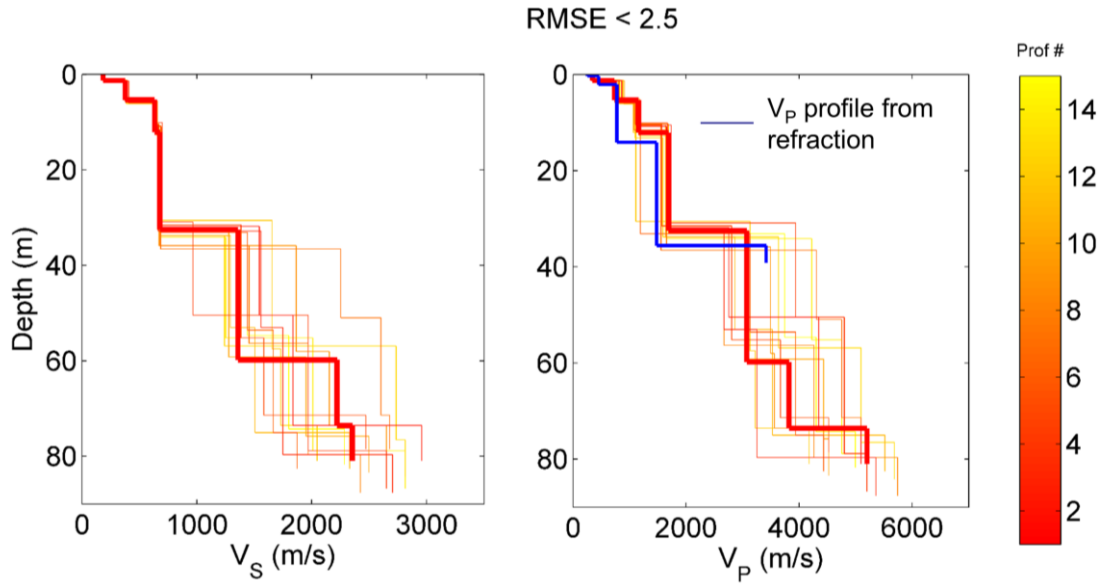


Figure 18 – Inversion results. Best 15 performing VS (left panel)/VP (right panel) profiles ($RMSE < 2.5$). Profiles are sorted according to RMSE (color scale). The lowest misfit model, selected as final result, is represented with a thicker line.

6.2 Quarter-wavelength representation

The quarter-wavelength velocity representation (Joyner et al., 1981) attributes to each frequency the average velocity at a depth equal to $\frac{1}{4}$ of the corresponding wavelength. It is a useful proxy in estimating the depth of reliable investigation of the available experimental data. In the presented case, the minimum frequency for the phase velocity data is 5.9 Hz, for the ellipticity curve is 1 Hz, which correspond to quarter-wavelength depths of 22 and 452 m, respectively (Figure 19, top panel). Figure 19, bottom panel, shows the quarter-wavelength impedance contrast (Poggi et al., 2012), which is the ratio between two quarter-wavelength average velocities, from the top and bottom part of the velocity profile respectively, at a given frequency. The graph shows a peak at the resonance frequency.

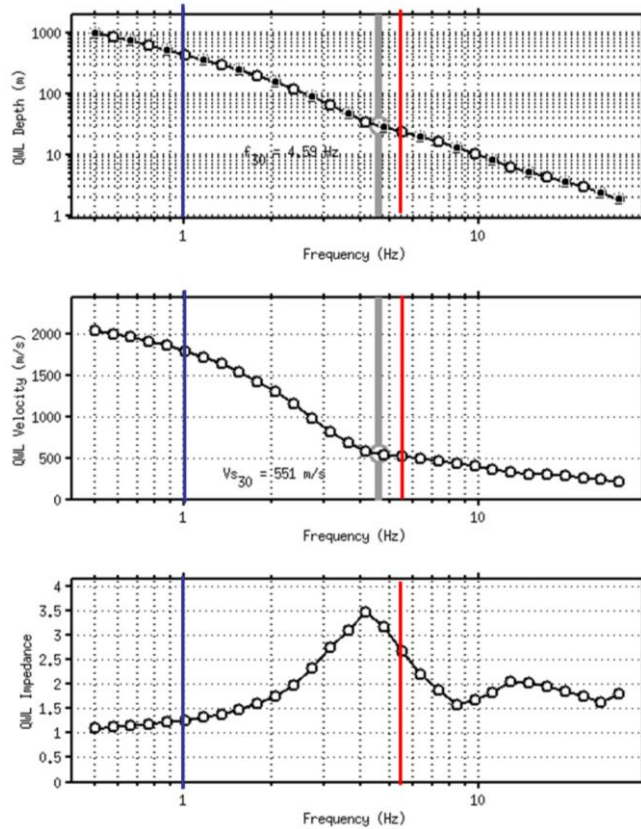


Figure 19 – Quarter-wavelength representation of the selected velocity profile. Top: depth; center: velocity; bottom: impedance contrast. The gray line in the top and center panel refers to V_{s30} . Blue and red lines in all panels define the depth of constrain for ellipticity and phase velocity data, respectively.

6.3 SH transfer function.

The theoretical SH-wave transfer function for vertical propagation (Roesset, 1970) was computed for the selected profile (Figure 20). The transfer function is corrected for the Swiss reference rock model (Poggi et al., 2011), following Edwards et al. (2013).

Unfortunately, as no useful events have been recorded so far by SFEL (due to the short time since installation), it is not possible to compare the computed SH transfer function with the amplification function obtained by empirical spectral modelling. Hence, the site characterization for SFEL site will be reassessed when this will be available.

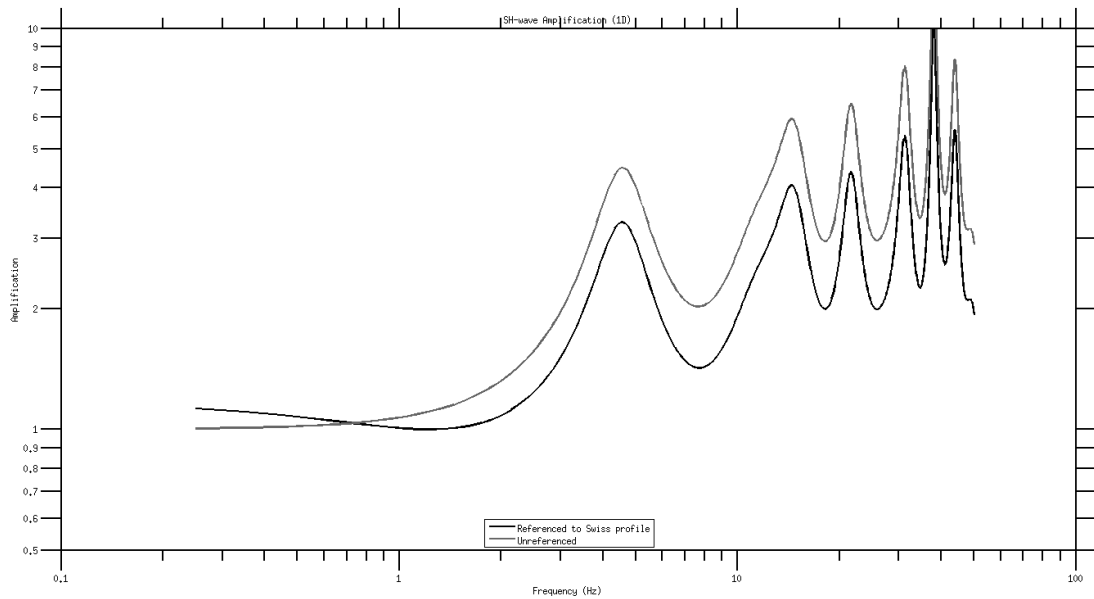


Figure 20 – Modeled SH transfer function from the selected velocity profile, corrected for the Swiss reference rock model.

7 Conclusions

Active seismic surveys and a single station noise recording were performed to characterize the structure of the subsurface below the SSMNet station SFEL. Active data were processed to derive a multimodal Rayleigh wave dispersion curve, and to extract the direct and refracted first break arrivals of P-waves. Passive data were analyzed to estimate the ellipticity curve of Rayleigh waves.

The velocity profile derived from the inversion process includes a surficial layer with $V_S = 183$ m/s and 1.2 m thick (soil cover); below, the gravelly alluvial terrace of the Aare is met (depth 1.2 – 32.5 m). The shallower portion of the alluvial terrace is constituted by gravel mixed with sand, silt and stones ($V_S = 377$ m/s, thickness 4 m), followed by more compacted gravels ($V_S=670$ m/s). The water table is probably located within this layer, at 12.1 m depth. The alluvial terrace rests on a formation of sand-/siltstone with clayey lenses ($V_S = 1357$ m/s): the impedance contrast with the overlying gravelly layers determines the fundamental peak at 5 Hz in the H/V curves. At depths greater than 60 m more compact rock layers are present ($V_S = 2200$ and 2353 m/s), which could be identified as dolomitic marble and the upper portion of the Gipskeuper formation.

The obtained V_{S30} is 551 m/s, thus classifying the soil as B type, according to Eurocode 8 (CEN, 2004) and SIA261 (SIA, 2014).

References

- Boiero, D., and L. V. Socco, 2010, Retrieving lateral variations from surface wave dispersion curves analysis: *Geophysical Prospecting*, **58**, 977–996
- Burjánek, J., C. Michel., G. Gassner-Stamm, V. Poggi, D. Roten, C. Cauzzi, and D. Fäh, 2013a. Grächen - Ausblick (SGRA) Site Characterization Report, Schweizerischer Erdbebendienst.
- Burjánek, J., C. Michel., G. Gassner-Stamm, V. Poggi, D. Roten, C. Cauzzi, and D. Fäh, 2013b. St. Niklaus, Bahnhofplatz (SNIB) Site Characterization Report, Schweizerischer Erdbebendienst.
- CEN, 2004. Eurocode 8: Design of structures for earthquake resistance – Part 1: general rules, seismic actions and rules for buildings. European Committee for Standardization, en 1998-1 edition.
- Edwards, B., Michel, C., Poggi, V., and Fäh, D. (2013). Determination of Site Amplification from Regional Seismicity : Application to the Swiss National Seismic Networks. *Seismological Research Letters*, 84(4).
- Fäh, D., F. Kind, and D. Giardini, 2001. A theoretical investigation of average H/V ratios. *GJI*, 145, no. 2, 535-549.
- Foti, S., Lai C.G., Rix G.J., and C. Strobbia, 2015, *Surface Wave Methods for Near-Surface Site Characterization*: CRC Press, Taylor & Francis Group LLC.
- Hobiger, M., P.-Y. Bard, C. Cornou, and N. Le Bihan, 2009. Single station determination of Rayleigh wave ellipticity by using the random decrement technique (RayDec). *GRL*, 36, L14303.
- Hobiger, M., C. Cornou, M. Wathelet, G. Di Giulio, B. Knapmeyer-Endrun, F. Renalier, P.-Y. Bard, A. Savvaidis, S. Hailemikael, N. Le Bihan, M. Ohrnberger, and N. Theodoulidis, 2013. Ground structure imaging by inversion of Rayleigh wave ellipticity: sensitivity analysis and application to European strong motion sites. *GJI*, 192, 207-229.
- Jäkli geologie, 2012. Projekt SwissFEL, Würenlingen (AG), SwissFEL Brunnen 1.
- Joyner, W. B., Warrick, R. E., and Fumal, T. E. (1981). The effect of Quaternary alluvium on strong ground motion in the Coyote Lake, California, earthquake of 1979. *Bulletin of the Seismological Society of America*, 71(4):1333–1349.
- Klinge, E., 2012. Sediment thickness of Switzerland. Federal Office of Topography swisstopo, SGPK.
- Maranò S., 2016. http://mercalli.ethz.ch/~marra/WaveDec/userguide_WaveDec.html

Maranò, S., Hobiger M., and D. Faeh, 2016. Analysis of Rayleigh Waves with Circular Wavefront: a Maximum Likelihood Approach. *GJI*, *under review*.

Michel, C., B. Edwards, V. Poggi., J. Burjánek, D. Roten, C. Cauzzi, and D. Fäh, 2014. Assessment of Site Effects in Alpine Regions through Systematic Site Characterization of Seismic Stations. *BSSA*, 104, no. 6, 2809-2826

Michel C., V. Poggi, C. Cauzzi, J. Burjánek, D. Roten, and D. Fäh, 2013, Lucerne – Bramberg (SLUB) Site Characterization Report. Schweizerischer Erdbebendienst.

NAGRA, 1985a. Technischer Bericht 85-01, Sondierbohrung Böttstein Untersuchungsbericht, Beilagenband A. Beiträge zur Geologie der Schweiz, geotechnische Serie, Lieferung 67, Schweizerische Geotechnische Kommission.

NAGRA, 1985b. Technischer Bericht 85-01, Sondierbohrung Boettstein Untersuchungsbericht, Beilagenband B. Beiträge zur Geologie der Schweiz, geotechnische Serie, Lieferung 67, Schweizerischen Geotechnischen Kommission.

Nakamura, Y., 1989. A Method for Dynamic Characteristics Estimation of Subsurface Using Microtremor on the Ground Surface. Quarterly Report of RTRI, vol. 30, no. 1, 25- 33.

Park, C. B., R. D. Miller, and J. Xia, 1999, Multichannel analysis of surface waves: *Geophysics*, **64**, 800–808.

Poggi, V., and D. Fäh, 2009. Estimating Rayleigh wave particle motion from three component array analysis of ambient vibrations. *GJI*, 180, no. 1, 251-267.

Poggi, V., Edwards, B., and Fäh, D. (2011). Derivation of a Reference Shear-Wave Velocity Model from Empirical Site Amplification. *Bulletin of the Seismological Society of America*, 101(1):258–274.

Poggi, V., Edwards, B., and Fäh, D. (2012). Characterizing the Vertical-to-Horizontal Ratio of Ground Motion at Soft-Sediment Sites. *Bulletin of the Seismological Society of America*, 102(6):2741–2756.

Poggi V., C. Michel, D. Roten, J. Burjánek, C. Cauzzi, and D. Fäh, 2013, Lucerne – Werkhofstrasse (SLUW) Site Characterization Report. Schweizerischer Erdbebendienst.

Redpath, B. B., 1973, Seismic refraction exploration for engineering site investigations: National Technical Information Service, Technical Report E-73-4.

Reynolds, J.M., 2011, An introduction to applied and Environmental Geophysics: John Wiley & Sons, Ltd.

Roesset, J. (1970). Fundamentals of soil amplification. In Hansen, R. J., editor, *Seismic Design for Nuclear Power Plants*, pages 183–244. M.I.T. Press, Cambridge, Mass.

SIA, 2014. SIA 261 Einwirkungen auf Tragwerke. Société Suisse des ingénieurs et des architectes, Zurich, Switzerland.

Socco, L.V., D. Boiero, S. Foti, and R. Wisen, 2009, Laterally constrained inversion of ground roll from seismic reflection records: *Geophysics*, **74**, no. 6, G35-G45.

Socco, L.V., and C. Strobbia, 2004, Surface-wave method for near-surface characterization: a tutorial: *Near Surface Geophysics*, **2**, no. 4, 165-185.

Swisstopo, Federal Office of Topography, 2013. *Geological Atlas of Switzerland 1:25000 (GA25)*.

Wathelet, M., 2008. An improved neighborhood algorithm: Parameter conditions and dynamic scaling. *GRL*, 35, no.9, 1-5.

Xia, J., R. D. Miller, C. B. Park, and G. Tian, 2003. Inversion of high frequency surface wave with fundamental and higher modes. *Journal of Applied Geophysics*, 52, 45-57.